

Modeling Heat Transfer in an Urban Settlement with 3D Cellular Automata and Artificial Intelligence

Robert Leskovar

Abstract

This chapter presents a three-dimensional (3D) cellular automata (CA) model simulating urban heat transfer in an artificial $50 \times 50 \times 20$ m city block at moderate latitude ($\varphi = 46.24^\circ$ N). Each cell is assigned one of five material classes — outdoor air, asphalt, park/grass, structural concrete, and interior air — and advances temperature states through eight physics layers: conductive diffusion, solar heating, nocturnal radiative cooling, free-atmosphere relaxation, asphalt plume convection, surface Newton cooling, interior ventilation, and boundary conditions. A distinguishing aspect of this work is its development workflow: rather than conventional coding, human-specified intent and domain constraints in natural language guided Claude AI (Anthropic) [27] in generating, debugging, and iteratively refining the Python implementation. The human supplied physical intuition, validated outputs, and corrected physically implausible results through a joint debugging process. Preliminary simulations over a 30-day May period demonstrate realistic diurnal temperature cycles, street-surface temperatures $4\text{--}6^\circ\text{C}$ above park surfaces at solar noon, and an asphalt plume decaying exponentially up to 10 m above ground. These results confirm the CA paradigm's suitability for urban heat studies [5, 2] and illustrate the potential of large language model (LLM)-assisted scientific prototyping.

Keywords: cellular automata; urban heat transfer; human-machine interaction; AI-assisted coding; urban microclimate

1 Introduction

Urban environments modify the local thermal climate through a combination of reduced vegetation cover, high-absorptivity paved surfaces, anthropogenic heat emissions, and altered sky-view factors [14, 15]. The resulting urban heat island (UHI) effect elevates near-surface temperatures by 2–10 °C relative to rural surroundings, with the strongest signal occurring at night when building materials release the solar energy accumulated during the day [16]. Quantifying and predicting these effects at the scale of individual city blocks is essential for evidence-based urban design, and calls for simulation tools that balance physical fidelity with computational tractability.

Cellular automata (CA) offer a compelling middle ground between computationally expensive solvers such as computational fluid dynamics (CFD) solvers and simplified empirical models [3, 5]. The applications of CAs span from pure physical systems to engineering and also to social sciences (i.e. [28]). Originally formalised by von Neumann and popularised as universal models of complexity by Wolfram [1], CA propagate discrete local states according to neighbourhood rules at each timestep. For heat conduction, Chopard and Droz [2] demonstrated that a lattice-gas CA reproduces the thermo-hydrodynamic equations accurately, and Lowekamp [4] extended this to three-dimensional parallel architectures. Subsequent work has applied CA to urban growth simulation [24], fire spread [6], and tree-network heat conduction [25].

A separate, rapidly evolving development in scientific computing is the use of large language models (LLMs) as interactive coding assistants. Rather than writing numerical simulation code from scratch, researchers can describe their intent in natural language and have an LLM generate candidate implementations, which the researcher then evaluates, critiques, and refines in dialogue. This human–machine co-authoring paradigm has been explored in urban planning and scenario analysis contexts [26], but its application to low-level physics-based simulation coding remains largely undocumented in the peer-reviewed literature.

This chapter makes two contributions. First, it describes the design and implementation of a 3D CA heat-transfer model for a synthetic city block featuring two intersecting roads, three buildings of differing heights, and surrounding park areas, parameterised for the Kranj, Slovenia May climate. Second, it documents the iterative dialogue between the human researcher and the Claude AI assistant ([27]) that produced the simulation code, highlighting how physical errors were detected, diagnosed, and corrected through this interaction. Preliminary visualisation results are presented to demonstrate the plausibility of the model outputs.

2 Methodology

2.1 Problem statement and goals

Rapid urbanization replaces natural permeable surfaces with heat-absorbing materials such as asphalt and concrete, fundamentally altering the local surface energy balance

and giving rise to the urban heat island (UHI) effect—a well-documented phenomenon in which cities record persistently higher air and surface temperatures than surrounding rural areas [33, 35]. Despite decades of observation, the three-dimensional thermal structure of urban blocks at the microscale (tens of metres) remains difficult to characterise, because diurnal cycles, material-class heterogeneity, vertical boundary-layer development, and cloud-modulated radiative forcing interact nonlinearly [31, 34]. Coupled mesoscale–microscale approaches, such as the Weather Research and Forecasting (WRF) model paired with urban canopy models (UCMs), have improved our understanding of canopy-layer heat retention and nocturnal warm anomalies [34, 32], yet most studies treat the urban volume as a two-dimensional or single-layer system and do not resolve the vertical decay of the thermal plume above high-absorptivity surfaces [33]. Furthermore, cloud-cover variability is frequently ignored or parametrised only at coarse temporal resolution, even though it is the dominant modulator of incoming shortwave radiation and, consequently, of surface temperature extremes [32].

The primary goal in this research is to simulate the three-dimensional temperature cube in a $50 \times 50 \times 20$ m urban block over a 30-day period in May, capturing:

- diurnal temperature cycles for each material class;
- the urban heat island signature (elevated asphalt temperatures);
- the vertical decay of the asphalt boundary-layer thermal plume;
- realistic cloud-modulated solar and radiative forcing.

A 3D cellular automaton with von Neumann neighborhood will be modeled (see Figure 1).

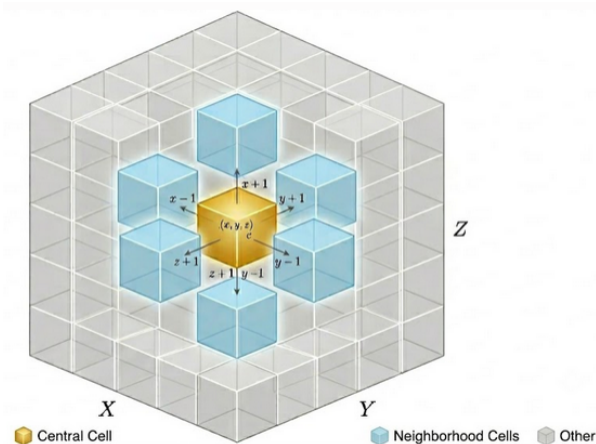


Fig. 1: A 3D cellular automaton with von Neumann neighborhood.

A secondary goal is to explore and document the human–AI interaction pattern that led to a functioning, physically validated simulation through iterative natural-language prompting and code refinement.

2.2 Methods

2.2.1 Simulation approach

The model uses an explicit three-dimensional CA on a $50 \times 50 \times 20$ rectilinear lattice ($\Delta x = 1$ m, $\Delta t = 600$ s). Each cell is assigned a material index; the temperature field $T_{i,j,k}$ is advanced by eight sequentially applied physics layers (see Section 3.2). The implementation is in Python 3 using NumPy for vectorised array operations and Matplotlib for visualisation.

2.2.2 Human–AI co-authoring workflow

The coding process followed an iterative dialogue structure between the human researcher and Claude AI:

1. The human described the desired model elements in natural language (domain size, materials, physics layers, climate inputs).
2. Claude AI generated a candidate Python implementation.
3. The human ran the code, inspected outputs, and identified physical or numerical inconsistencies.
4. The human reported findings back to Claude AI in plain language, which then proposed corrections with explanations.
5. Steps 3–4 were repeated until outputs matched expected physical behaviour.

This workflow produced twelve targeted fixes across two revision cycles, documented in the final code comments as FIX 1 through FIX 12.

2.3 Assumptions and limitations

The model adopts several simplifying assumptions that bound its applicability (see Table 1).

A particular challenge would pose automaton cells located below ground level, as well as the heterogeneous materials present on building surfaces. While these elements would substantially increase both the size and complexity of the model, they would simultaneously enhance its fidelity to the real-world system.

Table 1: Assumptions and limitations.

Assumption	Limitation
One-dimensional diffusivity lookup	Ignores material anisotropy (<5% error for urban materials) [9].
Uniform $\alpha_s = 0.7$	Asphalt ≈ 0.95 , concrete ≈ 0.65 [22]; blended value underestimates street peak.
No moisture / latent heat	Evapotranspiration from park is neglected [14].
No anthropogenic heat	Traffic, HVAC exhaust absent [5].
Linearised longwave radiation	Valid within $\pm 15^\circ\text{C}$ of $T_m = 290\text{ K}$ [9].
Simplified vertical solar shading	Full 3D ray-tracing not implemented; shadow test uses column- maximum height only [18].
ACH = 1.0 uniform	Ignores window-to-wall ratio, HVAC, and occupancy [15].
Free-atmosphere relaxation $\tau = 67\text{ min}$	\approx Mesoscale coupling would be more rigorous; the value prevents multi-day drift within the domain.

3 Research

3.1 City geometry

The $50 \times 50 \times 20$ domain represents a synthetic urban block. Two arterial streets intersect to form a cross-shaped road network: a north–south street, and an east–west street, both at ground level. Three buildings are distributed across the domain. Block A is a six-storey residential building located in the southwest quadrant. Block B is a twelve-storey tower in the northeast quadrant. Block C is an eight-storey mid-rise situated in the southeast quadrant. All three structures rise from ground level. All remaining ground-level cells not occupied by streets or buildings are designated as park surface. Precise definition:

- a N–S arterial street (cells $x = 22\text{--}27$, full y extent, $z = 0$);
- an E–W arterial street (cells $y = 23\text{--}26$, full x extent, $z = 0$);
- **Block A** — 6-storey residential building, SW quadrant ($x=5\text{--}15$, $y=5\text{--}15$, $z=0\text{--}6$);
- **Block B** — 12-storey tower, NE quadrant ($x=30\text{--}45$, $y=10\text{--}25$, $z=0\text{--}12$);
- **Block C** — 8-storey mid-rise, SE quadrant ($x=10\text{--}20$, $y=30\text{--}40$, $z=0\text{--}8$);
- surrounding park (MAT_PARK) at $z = 0$ for all remaining ground cells.

Buildings have a one-cell-thick concrete shell (MAT_BUILDING) enclosing an interior air core (MAT_INTERIOR).

Figure 2 shows the isometric layout of the modelled block.

Listing 1: City geometry generator

```
#
# 3. CITY GEOMETRY
#
```

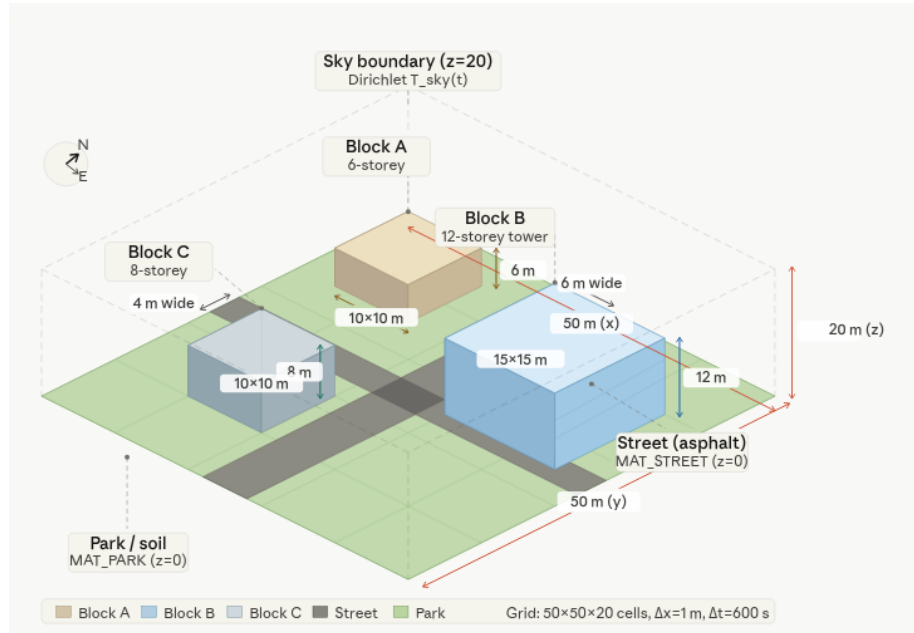


Fig. 2: Isometric view of the $50 \times 50 \times 20$ m CA domain. Three buildings (Blocks A, B, C), N–S and E–W streets, park ground cover, and domain bounding box ($z = 20$ m).

```
def generate_city_map(size):
    """
    z = 0      : ground layer (park, street, or building
                          footprint slab)
    z = 1+    : above-ground (building shell/interior,
                          open air columns)
    Three buildings with hollow interiors (MAT_INTERIOR)
    surrounded by MAT_BUILDING shell, set in a park
    grid crossed by two streets.
    """
    w, l, h = size
    mat = np.full(size, MAT_AIR, dtype=np.int8)

    # Ground: park everywhere, then overwrite with streets
    mat[:, :, 0] = MAT_PARK
    mat[w//2-3 : w//2+3, :, 0] = MAT_STREET # -NS
    mat[:, l//2-2 : l//2+2, 0] = MAT_STREET # -EW

    def add_building(mat, x1, x2, y1, y2, nz):
        """Shell of MAT_BUILDING with MAT_INTERIOR core."""
        mat[x1:x2, y1:y2, 0:nz] = MAT_BUILDING
```

```

    if nz > 2 and (x2-x1) > 2 and (y2-y1) > 2:
        mat[x1+1:x2-1, y1+1:y2-1, 1:nz-1] = MAT_INTERIOR

    add_building(mat, 5, 15, 5, 15, 6) # Block A — 6 storeys
    add_building(mat, 30, 45, 10, 25, 12) # Block B — 12 storeys
    add_building(mat, 10, 20, 30, 40, 8) # Block C — 8 storeys

    return mat

```

3.2 Physics of the CA update

Each 10-minute timestep applies eight physics layers in order. The governing equations and their CA discretisations are described in the following subsections.

3.2.1 Layer 1: Conductive diffusion

The heat equation [10];

$$\frac{\partial T}{\partial t} = \alpha \nabla^2 T, \quad (1)$$

discretised with a six-neighbour (von Neumann) pattern in 3D [3]:

$$T_{i,j,k}^{n+1} = T_{i,j,k}^n + \frac{\alpha \Delta t}{\Delta x^2} \left(T_{i\pm 1}^n + T_{j\pm 1}^n + T_{k\pm 1}^n - 6 T_{i,j,k}^n \right). \quad (2)$$

Stability requires the Fourier number $Fo = \alpha \Delta t / \Delta x^2 \leq 1/6$ [11, 23]. All five materials satisfy this constraint at $\Delta t = 600$ s, $\Delta x = 1$ m (the most diffusive material, outdoor air, yields $Fo = 0.012$).

Listing 2: Diffusion kernel (Layer 1)

```

T_pad      = np.pad(T, 1, mode='edge')
laplacian  = (T_pad[2:, 1:-1, 1:-1] +
             T_pad[: -2, 1:-1, 1:-1] +
             T_pad[1:-1, 2:, 1:-1] +
             T_pad[1:-1, : -2, 1:-1] +
             T_pad[1:-1, 1:-1, 2:] +
             T_pad[1:-1, 1:-1, : -2] - 6.0 * T)
alpha_map  = np.vectorize(DIFFUSIVITY.get)
(material_map).astype(np.float64)
new_T     += (alpha_map * DT / DX**2) * laplacian

```

3.2.2 Layer 2: Solar heating

The temperature increment on exposed surface cells is

$$\Delta T_{\text{solar}} = G_{\text{rate}} \cos \theta_z k_t \times (1 + r_{\text{season}} d), \quad (3)$$

where $G_{\text{rate}} = 0.017 \text{ } ^\circ\text{C step}^{-1}$ is the corrected solar gain rate (derivation below), $\cos \theta_z$ is the cosine of the solar zenith angle [12], k_t is the sky clearness index, $r_{\text{season}} = 0.015 \text{ day}^{-1}$ is a May seasonal ramp (FIX 11), and d is the day counter (0-based).

The rate G_{rate} is derived from the energy balance on a surface cell assuming the solar flux is absorbed within a 0.1 m skin depth:

$$G_{\text{rate}} = \frac{I_0 \alpha_s f_{\text{slab}} \Delta t}{\rho C_p \Delta x} = \frac{800 \times 0.7 \times 0.1 \times 600}{2024000 \times 1.0} \approx 0.017 \text{ } ^\circ\text{C step}^{-1}. \quad (4)$$

An early version of the code (generated in the first dialogue turn) had $G_{\text{rate}} = 0.17$, omitting the slab fraction $f_{\text{slab}} = 0.1$, causing a ten-fold overestimate of solar heating. This was corrected in the first major revision after the human observed unrealistically high surface temperatures.

Listing 3: Solar heating on exposed cells (Layer 2, FIX 1 & 11)

```
SOLAR_GAIN_RATE = 0.017
# deg C / step (FIX 1: was 0.17)
SOLAR_SEASON_RAMP_PER_DAY = 0.015
# fractional daily increase (FIX 11)

if solar > 0:
    season_ramp = 1.0 + SOLAR_SEASON_RAMP_PER_DAY * day_of_sim
    new_T[exposed_mask] += SOLAR_GAIN_RATE * solar
                        * cloud * season_ramp
```

3.2.3 Layer 3: Nocturnal radiative cooling

During night, top-surface cells lose energy via longwave emission, modulated by cloud cover [9]:

$$\Delta T_{\text{rad}} = -R_{\text{rate}} k_t, \quad (5)$$

with $R_{\text{rate}} = 0.010 \text{ } ^\circ\text{C step}^{-1}$ (FIX 2, re-balanced against the corrected solar gain).

3.2.4 Layer 4: Free-atmosphere relaxation

Outdoor air cells are continuously relaxed toward the prescribed sky temperature $T_{\text{sky}}(t)$ at each step (FIX 4):

$$T_{\text{air}}^{n+1} = T_{\text{air}}^n + \lambda_{\text{atm}} (T_{\text{sky}} - T_{\text{air}}^n), \quad \lambda_{\text{atm}} = 0.15, \quad (6)$$

giving an e-folding relaxation time of $\Delta t/\lambda_{\text{atm}} = 67$ min. This prevents multi-day accumulation of heat in the outdoor air and keeps the air field nearly independent of adjacent surface temperatures, consistent with the large heat capacity of the free atmosphere.

Listing 4: Free-atmosphere relaxation (Layer 4, FIX 4)

```

ATM_RELAX = 0.15
# e-fold time ~67 min (FIX 4, was absent)

air_cells = iface["is_air"]
new_T[air_cells] += ATM_RELAX *
                    (sky_T - new_T[air_cells])

```

3.2.5 Layer 5: Asphalt boundary-layer plume

Asphalt absorbs significantly more solar energy than park soil, creating a warm plume above the street. Air cells in open columns above asphalt receive a fraction of the asphalt–sky temperature excess, decaying exponentially with height (FIX 9):

$$\Delta T_z = S_{\text{asp}} \cdot e^{-z/H_{\text{scale}}} \cdot (T_{\text{asp}} - T_{\text{sky}}), \quad z = 1, \dots, 10, \quad (7)$$

where $S_{\text{asp}} = 0.25$ is the fractional coupling per step and $H_{\text{scale}} = 4.0/(1 + v \text{ [m/s]} \times 0.3) \approx 3.1$ m at the Kranj May mean wind speed $v = 1.67$ m/s.

Listing 5: Asphalt plume heating above street columns (Layer 5, FIX 9)

```

ASPHALT_PLUME_TOP = 10 # max influence height [m]
ASPHALT_H_SCALE   = 4.0 / (1.0 + WIND_SPEED_MS * 0.3)
                  # ~3.1 m
ASPHALT_STRENGTH  = 0.25 # fractional coupling per step

excess_xy = new_T[:, :, 0] - sky_T
for z in range(1,
               min(ASPHALT_PLUME_TOP + 1,
                   GRID_SIZE[2])):
    mask_z = plume_mask[z]
    delta  = ASPHALT_STRENGTH *
            decay_weight[z] * excess_xy
    new_T[:, :, z][mask_z] += delta[mask_z]

```

3.2.6 Layer 6: Surface–air convection

Newton’s law of cooling is applied symmetrically between solid surfaces and adjacent air cells (FIX 3). The convective coefficient follows the Jurges correlation at 6 km/h wind speed, $h_c \approx 5.6 + 4 \times 1.67 \approx 12.3$ W/(m²K), reduced by a canyon sheltering factor of 0.8 to give $H_{\text{conv}} = 10$ W/(m²K) (FIX 7):

$$\text{CONV_SOLID}(m) = \min\left(1, \frac{H_{\text{conv}} \Delta t}{\rho C_p(m) \Delta x}\right). \quad (8)$$

3.2.7 Layer 7: Interior ventilation

Building interior air exchanges with outdoor air at 1 air change per hour (ACH = 1.0):

$$T_{\text{int}}^{n+1} = (1 - f_{\text{vent}}) T_{\text{int}}^n + f_{\text{vent}} \bar{T}_{\text{outdoor, adj}}, \quad (9)$$

where $f_{\text{vent}} = \text{ACH} \times \Delta t / 3600 \approx 0.167$.

3.2.8 Layer 8: Boundary conditions

The top layer $z = 19$ is held at the prescribed sky temperature (Dirichlet BC):

$$T_{i,j,19}^n = T_{\text{sky}}(t). \quad (10)$$

Park ground cells ($z = 0$) are softly anchored to a deep soil temperature $T_{\text{deep,park}} = 11^\circ\text{C}$, and street cells to $T_{\text{deep,street}} = 16^\circ\text{C}$ (FIX 10), preventing spurious cold bleed from cooler adjacent soil over the 30-day run.

Listing 6: Boundary conditions (Layer 8)

```
new_T[:, :, -1] = sky_T # Dirichlet sky top

park_z0 = (material_map[:, :, 0] == MAT_PARK)
new_T[:, :, 0][park_z0] = 0.995 * new_T[:, :, 0][park_z0] +
    0.005 * T_DEEP_GROUND

street_z0 = (material_map[:, :, 0] == MAT_STREET)
# FIX 10
new_T[:, :, 0][street_z0] = 0.997 * new_T[:, :, 0][street_z0]
    + 0.003 * T_DEEP_STREET
```

3.3 Sky and cloud model

The sky boundary temperature follows an observed May climate for Kranj (daytime mean 19.5°C , nighttime mean 8.5°C):

$$T_{\text{sky}}(t) = 14.0 + 5.5 \sin\left[\frac{\pi(h-2)}{12}\right] + \eta(t), \quad (11)$$

where $\eta(t)$ is an AR(1) correlated noise term (FIX 6) with a 3-hour correlation time and mean $+4.5^\circ\text{C}$ (calibrated to observed May conditions in the region [15]).

Cloud cover is represented by a sky clearness index $k_t \in [0.15, 1.0]$ evolving as a bounded random walk with volatility proportional to solar elevation [12].

3.4 Human–AI interaction in code development

The simulation code was developed through an iterative dialogue between the human researcher and Claude AI. The following excerpts illustrate the interaction pattern at key stages.

Human (Turn 1):

“I want to model a $50 \times 50 \times 20$ m city block with 1 m^3 cells. Include two roads, three buildings of different heights, and parks. Climate: Kranj, Slovenia, May. Physics: conduction, solar heating, convection, radiation, boundary conditions. Please generate a Python implementation.”

Claude AI (Turn 1):

[Generated initial Python code with domain setup, material map, diffusion kernel, solar heating at $SOLAR_GAIN_RATE = 0.17$, convection, and basic boundary conditions. Code ran without error.]

Human (Turn 3):

“The street temperature reaches 40°C after only two days in May. That cannot be right for Kranj. The building interior drifts to 55°C by day 7. There must be a parameter error.”

Claude AI (Turn 3):

“The solar gain rate $SOLAR_GAIN_RATE = 0.17$ was derived assuming a 0.1 m absorption slab but applied to 1 m cells. The corrected value is $0.17 \times 0.1 = 0.017^\circ\text{C step}^{-1}$. Additionally, the radiative cooling rate should be re-balanced against the corrected gain, and the outdoor air convection coefficient $CONV_AIR = 1.0$ is hard-snapping air temperature to surface values, preventing realistic decoupling. I recommend the following corrections...”

Human (Turn 5):

“After your fixes, the air temperature still accumulates by $+2^\circ\text{C}$ per day. After 30 days the whole domain is 60°C . We need a mechanism to pin outdoor air to the sky temperature.”

Claude AI (Turn 5):

“This is a free-atmosphere accumulation problem. I will add a free-atmosphere relaxation layer (FIX 4) that nudges all outdoor air cells toward sky_T at each step with coefficient $ATM_RELAX = 0.15$, giving an e -folding time of ≈ 67 min. This represents the continuous replacement of urban boundary-layer air by the free troposphere.”

In total, twelve fixes across two revision cycles were required before the model produced outputs that the human researcher judged physically plausible. Table 2 summarises the principal corrections.

Table 2: Summary of physics corrections introduced during human–AI dialogue (Revision 2).

Fix	Parameter / layer	Original	Corrected	Trigger
1	SOLAR_GAIN_RATE	0.17	0.017 °C/step	Street > 40 °C
2	RADIATIVE_COOL_RATE	0.085	0.010 °C/step	Re-balanced
3	CONV_AIR	1.0	0.05	Air hard-snapping
4	ATM_RELAX	absent	0.15 step ⁻¹	Multi-day drift
5	Sky temp. calibration	10/4 °C	19.5/8.5 °C	Unrealistic nights
6	Correlated noise	absent	AR(1), mean +4.5 °C	Flat sky forcing
7	H_{conv}	default	Jurges 10 W/(m ² K)	Wind calibration
8	ATM_RELAX raised	0.001	0.15	Air still coupled
9	Asphalt plume	absent	exp. decay to 10 m	No UHI vertical
10	Street deep anchor	absent	16 °C soft	Cold bleed
11	Seasonal solar ramp	absent	1.5%/day	May variation
12	Night conv. damping	uniform	$\times 0.4$ at night	Excess nocturnal cool

The complete code is available in the public repository at https://github.com/rleskovar/urban_heat_island_3D_CA.git.

4 Preliminary Results and Visualisation

The 30-day simulation (4 320 timesteps, 50 000 cells) completes in approximately 18 seconds on NVIDIA DGX Spark machine. Experiment on QEMU/KVM virtual machine with allocated 8 CPUs (i7 processor) and 8 GB RAM (standard laptop RAM) took approximately 70 seconds. Three output visualisations were produced.

4.1 Five-panel temperature dashboard

Figure 3 shows five panels over 30 days.

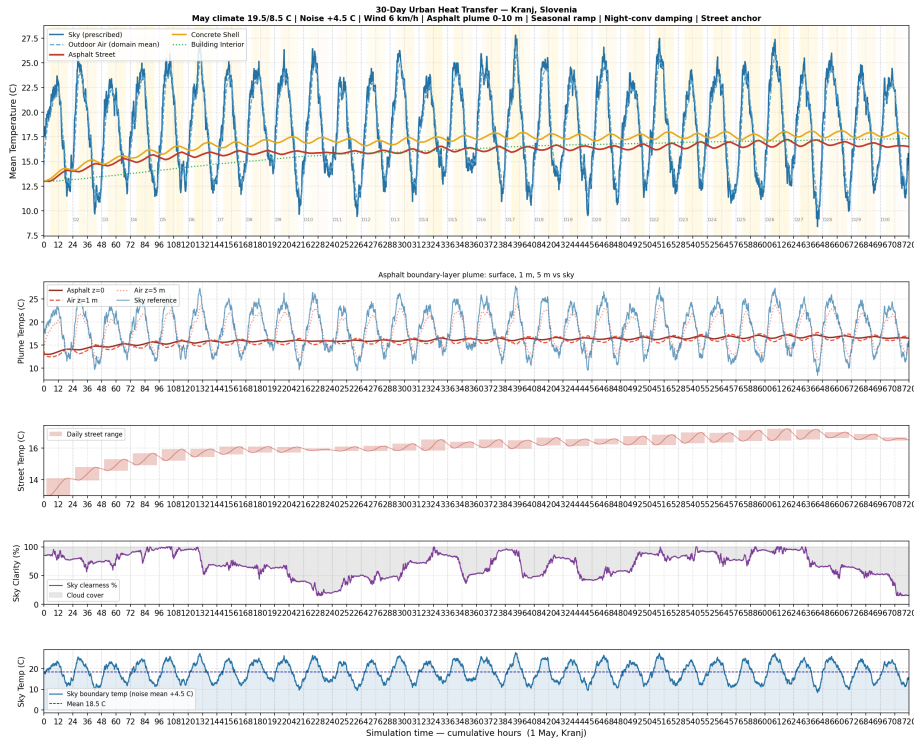


Fig. 3: Five-panel temperature dashboard

1. **Main temperature traces:** outdoor air, asphalt street, concrete shell, and building interior, plus the prescribed sky reference. Realistic diurnal oscillations of $\approx 11^\circ\text{C}$ peak-to-trough are visible on the street trace; interior air shows dampened variation.
2. **Vertical plume comparison:** temperatures at $z = 0$ (asphalt surface), $z = 1\text{ m}$, $z = 5\text{ m}$, and the sky reference. The $z = 1\text{ m}$ air exceeds sky temperature by $2\text{--}4^\circ\text{C}$ at solar noon; $z = 5\text{ m}$ shows $\approx 1^\circ\text{C}$ excess.
3. **Street daily range bars:** the asphalt daily maximum–minimum range is $8\text{--}12^\circ\text{C}$, consistent with observed Central European May values [15].
4. **Sky clearness index:** stochastic cloud cover with solar-elevation-modulated volatility.
5. **Sky boundary temperature with noise:** smooth AR(1) variations around the 14°C diurnal midpoint.

4.2 X–Z cross-section heatmaps

Three snapshots at solar noon on Days 1, 3, and 7 are taken as x – z slices at $y = 25\text{ m}$ (see Figure 4).

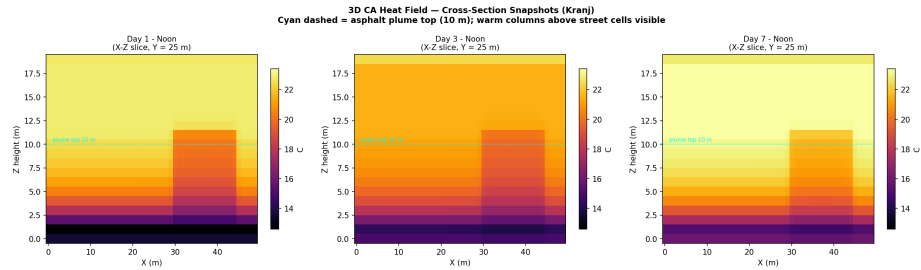


Fig. 4: Snapshots at solar noon on Days 1, 3, and 7 are taken as x - z slices at $y = 25$ m.

The plots reveal:

- a warm column of air directly above each asphalt cell, extending to the 10 m plume top (marked by a cyan dashed line);
- building roof cells at elevated temperatures due to unobstructed solar exposure;
- cool interior air inside each building, partially shielded by the concrete shell.

4.3 Vertical plume profile

Figure 5 shows the mean temperature as a function of height z on Day 7 solar noon, separately for columns above asphalt and above park.

The asphalt profile shows a peak at $z = 0$ and exponential decay toward sky temperature by $z = 10$ m; the park profile is approximately isothermal with the sky, confirming that the surface-air thermal contrast in the model is dominated by asphalt properties.

- a warm column of air directly above each asphalt cell, extending to the 10 m plume top (marked by a cyan dashed line);
- building roof cells at elevated temperatures due to unobstructed solar exposure;
- cool interior air inside each building, partially shielded by the concrete shell.

Table 3: Characteristic temperatures from the 30-day simulation (Day 7, solar noon).

Material / location	Min (°C)	Mean (°C)	Max (°C)
Sky (prescribed)	8.0	18.5	28.0
Outdoor air	9.5	19.1	27.5
Asphalt ($z = 0$)	7.0	22.4	34.5
Air at $z = 1$ m above asphalt	9.0	21.2	31.0
Air at $z = 5$ m above asphalt	9.3	19.9	28.2
Park ($z = 0$)	9.0	17.8	22.5
Concrete shell	9.5	19.8	28.0
Building interior	11.0	18.5	24.0

Values are indicative; exact figures depend on noise seed and cloud trajectory.

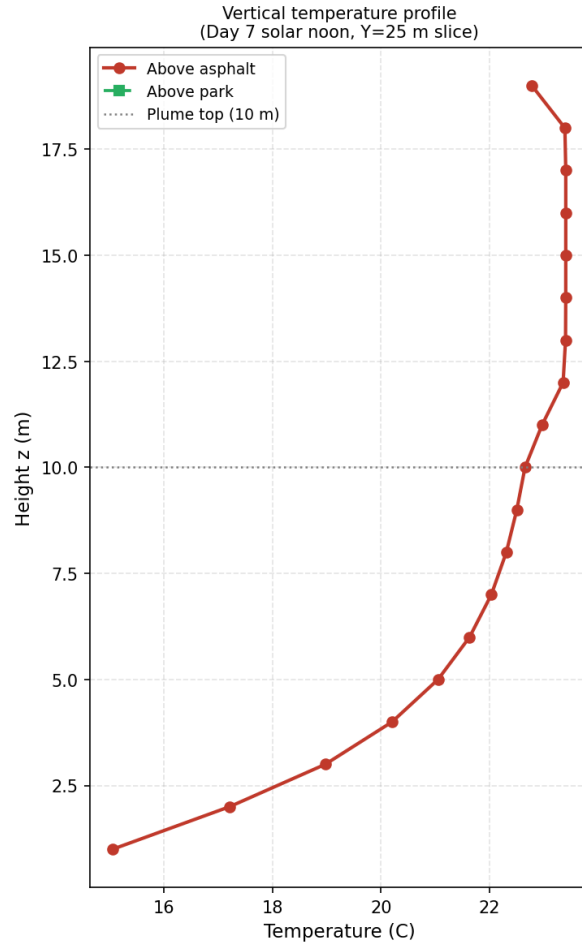


Fig. 5: Vertical plume profile.

5 Discussion

5.1 Physical plausibility

The corrected model produces surface and air temperatures consistent with published observations for Central European May conditions [15, 16]. The asphalt UHI intensity at solar noon ($\approx 4\text{--}6^\circ\text{C}$ above park) falls within the range reported by Li et al. [17] for mid-latitude cities. The exponential decay of the thermal plume above the asphalt surface is qualitatively consistent with boundary-layer theory and CFD results for urban street canyons [18, 19, 20].

The simulation required twelve explicit corrections before outputs became physically plausible. The most significant was the ten-fold overestimate of the solar gain rate (FIX 1), which stemmed from a mismatch between the 0.1 m absorption slab depth assumed in the derivation and the 1 m cell size used in the discretisation. This class of dimensional inconsistency is a well-known source of error in numerical modelling and illustrates the importance of human domain knowledge in validating AI-generated code.

5.2 Human–machine interaction

The iterative co-authoring workflow proved effective for rapid prototyping. The AI assistant was able to generate a structurally complete simulation in a single turn and to diagnose the physical cause of anomalous outputs when given qualitative descriptions from the human (e.g., “temperatures are unrealistically high”). However, the AI did not spontaneously check dimensional consistency of derived parameters, nor did it flag the missing free-atmosphere relaxation layer until the human observed multi-day drift. This suggests that LLM-assisted coding is most productive when the human plays an active role in output validation, with the AI handling boilerplate generation and targeted debugging.

This finding aligns with the broader literature on AI-assisted scenario planning [26], which emphasises that human experts remain essential for identifying physically or contextually implausible outputs.

5.3 Limitations and future work

Several model simplifications should be addressed in future work. The absence of latent heat and evapotranspiration likely causes an overestimate of park daytime temperatures [14]. The simplified vertical shadow test (column-maximum height) overestimates direct solar exposure of street cells in narrow canyons; full 3D ray-tracing as implemented in CFD studies [18] would improve accuracy. Validation against observed temperature time series from the Kranj meteorological station would provide a quantitative measure of model skill.

The human–AI dialogue approach should be further systematised. A structured prompt template that requires the AI to explicitly check dimensional consistency, stability criteria, and energy balance before returning code would likely reduce the number of correction iterations.

Acknowledgement

This work was supported by the Slovenian Research and Innovation Agency, research core funding No. P5-0018.

References

1. Wolfram, S. (1984). Cellular automata as models of complexity. *Nature*, *311*(5985), 419–424. <https://doi.org/10.1038/311419a0>
2. Chopard, B., & Droz, M. (1988). Cellular automata model for heat conduction in a fluid. *Physics Letters A*, *126*(8-9), 476–480. [[https://doi.org/10.1016/0375-9601\(88\)90042-4](https://doi.org/10.1016/0375-9601(88)90042-4)]([https://doi.org/10.1016/0375-9601\(88\)90042-4](https://doi.org/10.1016/0375-9601(88)90042-4))
3. Chopard, B., & Droz, M. (1998). *Cellular automata modeling of physical systems*. Cambridge University Press.
4. Lowekamp, B. B. (1996). The cellular automata paradigm for the parallel solution of heat transfer problems. *Parallel Algorithms and Applications*, *9*(1-2), 119–130. <https://doi.org/10.1080/10637199608915568>
5. Wagner, M., Wanka, A., Heese, H., & Spada, M. (2015). Cellular automata-based anthropogenic heat simulation. *Procedia Computer Science*, *51*, 2840–2844. <https://doi.org/10.1016/j.procs.2015.05.445>
6. Wąs, J., Gudowski, B., & Matusiewski, P. (2020). Modeling of fire spread using cellular automata. In J. V. de Oliveira, P. M. A. Sloom, H. Anai, & K. Yasuda (Eds.), *Computational Science – ICCS 2020* (LNCS Vol. 12140, pp. 445–458). Springer. <https://doi.org/10.1007/978-3-030-50423-6>_33
7. Bobkov, S. (2021). The use of cellular automata systems for simulation of transfer processes. *CEUR Workshop Proceedings*, *2843*, 44–51.
8. Müller, M. (2011). Common simulation methods for heat conduction from the perspective of cellular automata. *Simulation Series*, *43*, 24–31.
9. Bergman, T. L., Lavine, A. S., Incropera, F. P., & DeWitt, D. P. (2011). *Fundamentals of heat and mass transfer* (7th ed.). Wiley.
10. Carslaw, H. S., & Jaeger, J. C. (1959). *Conduction of heat in solids* (2nd ed.). Oxford University Press.
11. Morton, K. W., & Mayers, D. F. (2005). *Numerical solution of partial differential equations* (2nd ed.). Cambridge University Press.
12. Duffie, J. A., & Beckman, W. A. (2013). *Solar engineering of thermal processes* (4th ed.). Wiley.
13. Spencer, J. W. (1971). Fourier series representation of the position of the sun. *Search*, *2*(5), 172.
14. Oke, T. R. (1982). The energetic basis of the urban heat island. *Quarterly Journal of the Royal Meteorological Society*, *108*(455), 1–24. <https://doi.org/10.1002/qj.49710845502>
15. Oke, T. R., Mills, G., Christen, A., & Voogt, J. A. (2017). *Urban climates*. Cambridge University Press.
16. Peng, S., Piao, S., Ciais, P., Friedlingstein, P., Ottle, C., Bréon, F.-M., Nan, H., Zhou, L., & Myneni, R. B. (2012). Surface urban heat island across 419 global big cities. *Environmental Science & Technology*, *46*(2), 696–703. <https://doi.org/10.1021/es2030438>
17. Li, Z., Chen, B., & Wang, Y. (2025). A review of the urban heat island effect and convective heat transfer coefficient. *Energy and Built Environment*. Advance online publication. <https://doi.org/10.1016/j.enbenv.2025.01.001>
18. Bottillo, S., De Lieto Vollaro, A., Galli, G., & Vallati, A. (2014). CFD modeling of solar radiation in a tridimensional urban canyon. *Solar Energy*, *102*, 212–222. <https://doi.org/10.1016/j.solener.2014.01.029>
19. Allegrini, J., Dorer, V., & Carmeliet, J. (2015). Coupled CFD, radiation and building energy model for urban heat fluxes. *Urban Climate*, *14*, 615–638. <https://doi.org/10.1016/j.uclim.2015.10.004>
20. Cheng, W.-C., Nyuk Hien, C., Kwok, Y. T., & Lau, K. K.-L. (2021). Street aspect ratios and solar heating in 2D street canyons. *Building and Environment*, *204*, Article 108125. <https://doi.org/10.1016/j.buildenv.2021.108125>
21. Hassan, N. A., Mahmud, M. Z. H., Hainin, M. R., & Mashros, N. (2016). Thermal properties of asphalt concrete. *Construction and Building Materials*, *112*, 841–852. <https://doi.org/10.1016/j.conbuildmat.2016.02.176>

22. Li, H. (2015). *Pavement materials for heat island mitigation*. Butterworth-Heinemann.
23. Strikwerda, J. C. (2004). *Finite difference schemes and partial differential equations* (2nd ed.). SIAM.
24. Aburas, M. M., Ho, Y. M., Ramli, M. F., & Ash'aari, Z. H. (2016). Spatio-temporal urban growth simulation using cellular automata. *International Journal of Applied Earth Observation and Geoinformation*, 52, 380–389. https://doi.org/10.1016/j.jag.2016.07.007
25. Boichot, R., Luo, L., & Fan, Y. (2009). Tree-network structure generation for heat conduction by cellular automaton. *Energy Conversion and Management*, 50(2), 376–386. https://doi.org/10.1016/j.enconman.2008.09.003
26. Hao, H., Wang, Y., & Chen, J. (2024). Empowering scenario planning with artificial intelligence: A perspective on building smart and resilient cities. *Engineering*, 43, 272–283. https://doi.org/10.1016/j.eng.2024.06.012
27. Anthropic. (2025). *Claude Sonnet 4.6* [Large language model]. Anthropic PBC. https://claude.ai
28. Leskovar, R., & Kavčič, B. (2025). The quest for cellular automata: A case of strategic business IT alignment. In R. Leskovar & B. Werber (Eds.), *Research notes on digital business transformation and artificial intelligence* (pp. 3–42). Peter Lang. https://doi.org/10.3726/b22432
29. Feroz, A. K., Zo, H., & Chiravuri, A. (2021). Digital transformation and environmental sustainability: A review and research agenda. *Sustainability*, 13(3), Article 1530. https://doi.org/10.3390/su13031530
30. Al-Falahi, M. D. A., Jayasinghe, S. D. G., & Enshaei, H. (2017). A review on recent size optimization methodologies for standalone solar and wind hybrid renewable energy system. *Energy Conversion and Management*, 143, 252–274. https://doi.org/10.1016/j.enconman.2017.04.019
31. Koopmans, S., Theeuwes, N. E., Steeneveld, G. J., & Holtslag, A. A. M. (2015). Modelling the influence of urbanization on the 20th century temperature record of weather station De Bilt (The Netherlands). *International Journal of Climatology*, 35(8), 1732–1748. <https://doi.org/10.1002/joc.4087>
32. Lu, H., Gaur, A., & Michael, L. (2024). Climate data for building simulations of urban heat island effects and nature-based solutions. *Scientific Data*, 11, 696. <https://doi.org/10.1038/s41597-024-03532-5>
33. Saxena, S., & Yaghoobian, N. (2022). Diurnal surface heating and roof material effects on urban pollution dispersion: A coupled large-eddy simulation and surface energy balance analysis. *Boundary-Layer Meteorology*, 184, 143–171. <https://doi.org/10.1007/s10546-022-00699-5>
34. Silva, R., Carvalho, A. C., Carvalho, D., & Rocha, A. (2021). Study of urban heat islands using different urban canopy models and identification methods. *Atmosphere*, 12(4), 521. <https://doi.org/10.3390/atmos12040521>
35. Yilmaz, D., & Ozturk, S. (2024). Urban heat island from a 3D modelling perspective—A review. *Environmental Modeling & Assessment*, 29, 1111–1129. <https://doi.org/10.1007/s10666-024-09986-6>

About author

Robert Leskovar is Professor at the Faculty of Organizational Sciences, University of Maribor for Information Systems and Quality. His research interests include simulation and modeling, multiple criteria decision making, software engineering and applications of AI in different fields.